Contents lists available at ScienceDirect

Journal of Nuclear Materials

journal homepage: www.elsevier.com/locate/jnucmat

Microstructural evolution of ion-irradiated commercially pure titanium

A. Amroussia [a,b], C.J. Boehlert [b,*], F. Pellemoine [c], D. Grummon [b], W. Mittig [d,e], T.R. Bieler [b], M. Li [f], W.-Y. Chen [f]

[a] Saint-Gobain Research Paris, Aubervilliers, France, 12309
[b] Michigan State University, East Lansing, MI, 48824
[c] Fermilab, Batavia, IL, 60510
[d] Facility for Rare Isotope Beams, East Lansing, MI, 48824
[e] National Superconducting Cyclotron Laboratory, East Lansing, MI, 48824
[f] Intermediate Voltage Electron Microscopy (IVEM)-Tandem Facility, Argonne National Laboratory, Lemont, IL, 60439

ARTICLE INFO

Keywords:
titanium
irradiation, ionization, microstructure, dislocations

ABSTRACT

Radiation-induced dislocation loop evolution in ion-irradiated commercially pure (CP) Ti was investigated through both ex situ 4 MeV Ar beams and by in situ TEM irradiation with 1 MeV Kr ion beams at different temperatures. The dominant mechanism for dislocation loop growth was loop coalescence. Both <a>- and c-component loops exhibited an increase in size and density with increased irradiation dose and temperature. C-component loops were observed only after reaching a threshold incubation dose (TID). In CP Ti, these loops initiated at lower doses compared to previous observations in Zr, and the TID decreased with increasing temperature.

1. Introduction

Titanium (Ti) alloys are widely used in the biomedical, aerospace and automotive industry due to their high specific strength, excellent fatigue and creep properties, corrosion resistance, good workability and weldability, as well as their commercial availability. Ti-alloys are also attractive for nuclear applications thanks to their compatibility with coolants (lithium, helium, water) and low activation in radioactive environments [1]. As a result, Ti-6Al-4V(wt.%)[1] is currently used as beam window material for high-intensity proton accelerators [2] and investigated as beam dump material for the Facility for Rare Isotope Beams at Michigan State University [3,4]. Several studies have investigated radiation damage in conventionally manufactured Ti and Ti-alloys, using electrons [5], neutrons [6,7], protons [2,8–10] and heavy ions [3, 11–14] for doses lower than 9 dpa (displacement per atom). The microstructural evolution of the irradiated hexagonal close packed (hcp) materials, such as α-phase Ti, depends on the anisotropy of the interstitial diffusion and is linked to the c/a ratio, where it is weakest for ratios close to $(\sqrt{3})$ [15,16]. For Ti the c/a ratio is 1.586 and basal loops are not expected. Experimentally, this rule was proven to be inaccurate for Ti [7] and other hcp materials like Zr [17] as both basal and prismatic loops were observed [5,7,18,19]. At low irradiation doses, black dots and prismatic <a>-type dislocation loops, which are mainly interstitial, were observed in Ti-alloys [18] and are thought to contribute significantly to radiation hardening[6,10,13,20]. Vacancy basal <c>-component loops were reported at higher dose levels [5,19] and are linked to irradiation-induced swelling [7,21].

In previous studies, only the final microstructure, after irradiation at a certain dose level, was investigated, precluding a deeper understanding of the evolution of the damage structures at different doses and temperatures. The current work focused on the nucleation of radiation-induced dislocation loops and their accumulation at higher doses. *In situ* transmission electron microscopy (TEM) irradiation was used as it can offer the capability to investigate the radiation damage evolution through continual imaging and allow for quantitative and qualitative microstructural studies [21–24].

The primary objective in this paper is to obtain a deeper understanding of the microstructural evolution in ion-irradiated commercially pure (CP) Ti in order to eventually accurately model its mechanical behaviour. To that end, a microstructural study was undertaken to provide both quantitative data on defect formation and defect densities, as well as qualitative information on defect interactions and growth

* Corresponding author.
E-mail address: boehlert@egr.msu.edu (C.J. Boehlert).

[1] Henceforth all alloy compositions are provided in weight percent unless otherwise indicated.

https://doi.org/10.1016/j.jnucmat.2024.155105
Received 15 November 2023; Received in revised form 15 April 2024; Accepted 16 April 2024

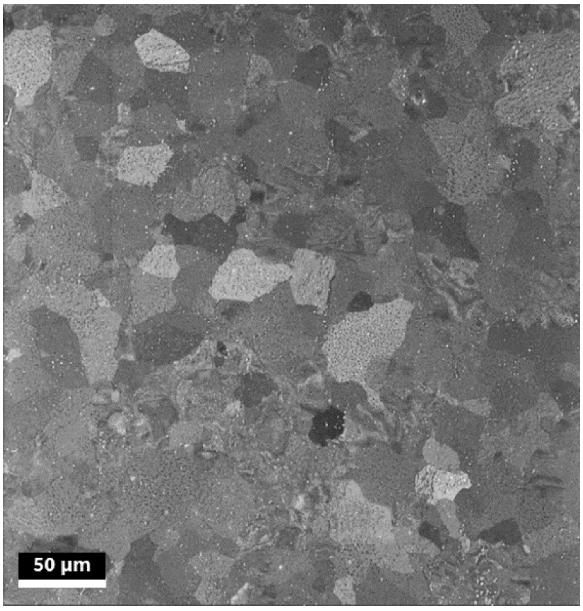

Fig. 1. Secondary electron SEM image showing the representative microstructure of the studied CP Ti.

mechanisms.

2. Experimental methods

2.1. Material

A description of the Grade 2 CP Ti material used in this study, which was provided by the National Energy Technology Laboratory (NETL) in Albany, Oregon, can be found in [25]. A 150 mm diameter ingot was triple vacuum arc remelted and then upset forged, forge flattened, and squared before rolling. The forging steps were performed at temperatures above the β-transus temperature, while the rolling passes were performed at temperatures below the β transus.

2.2. Sample preparation

2.2.1. Metallography and Electron Microscopy

Samples were mechanically polished using silicon carbide planar grinding papers from 600 up to 4000 grit. To achieve a mirror finish, the samples were polished between 1 and 2 hours with a chemical etchant composed of 1 part H_2O_2 to 5 parts Struers OP-S colloidal silica (0.04 µm). Scanning electron microscopy (SEM) and electron backscattered diffraction (EBSD) were performed on the metallographically prepared samples using a Tescan Mira III SEM at 20 keV. EBSD was performed using EDAX-TSL, Inc (Mahwah, NJ) version 6.1 OIM Data Acquisition and Analysis software. The scanning step size was between 0.3 and 0.5 µm for the α-phase with a typical 70° incidence angle. The average grain size was measured using the line intercept method [26]. Energy Dispersive Spectroscopy (EDS) was performed using a Tescan Mira III SEM at 15keV together with an EDAX-TSL EDS system. Transmission electron microscopy (TEM) and Energy Dispersive Spectroscopy (EDS) were performed using a Talos F200X (Scanning)-TEM at the Center for Nanoscale Materials (CNM), Argonne National Laboratory, IL, USA.

2.2.2. TEM sample preparation

After grinding the CP Ti to a thickness between 100 and 150 µm, 3 mm diameter discs were punched and then electropolished using a Struers Tenupol 5 twin-jet electropolisher at a temperature between -44 °C and -30 °C. A solution bath of 300 mL methanol, 175 mL 2-butanol, and 30 mL perchloric acid was used. The thickness of the thin area in the TEM foils was estimated to be 100 nm. Low keV ion milling was performed as the last step to remove contaminants and improve TEM foil quality. The beam energy was held between 2 and 3 keV and the milling angle varied incrementally between 8° to 4°.

For material irradiated ex situ, the samples were thinned after irradiation to a thickness between 100 and 150 µm by mechanical grinding on the unirradiated side only. The irradiated surface was covered by Lacomit Varnish (Agar Scientific Ltd) to prevent material removal from the irradiated side during the electropolishing step. Low keV ion milling was also performed to remove contaminants and improve TEM foil quality.

2.3. Microstructural characterization of the unirradiated material

A representative SEM image and an EBSD orientation map of the studied CP Ti are provided in Figs. 1 and 2, respectively. The microstructure, which was not strongly textured, consisted of α-phase grains,

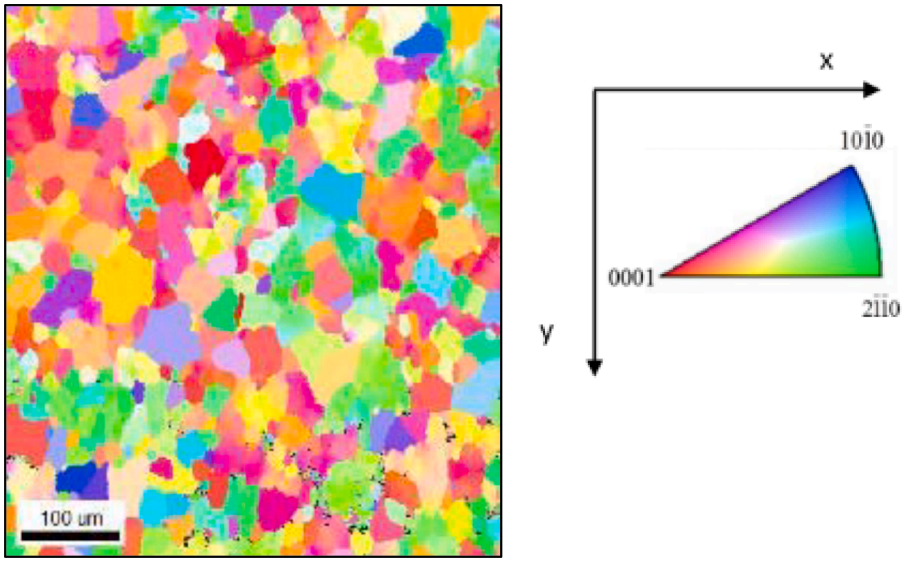

Fig. 2. EBSD inverse pole figure (IPF) map of the studied CP Ti with the corresponding sample normal direction inverse pole figure unit triangle.

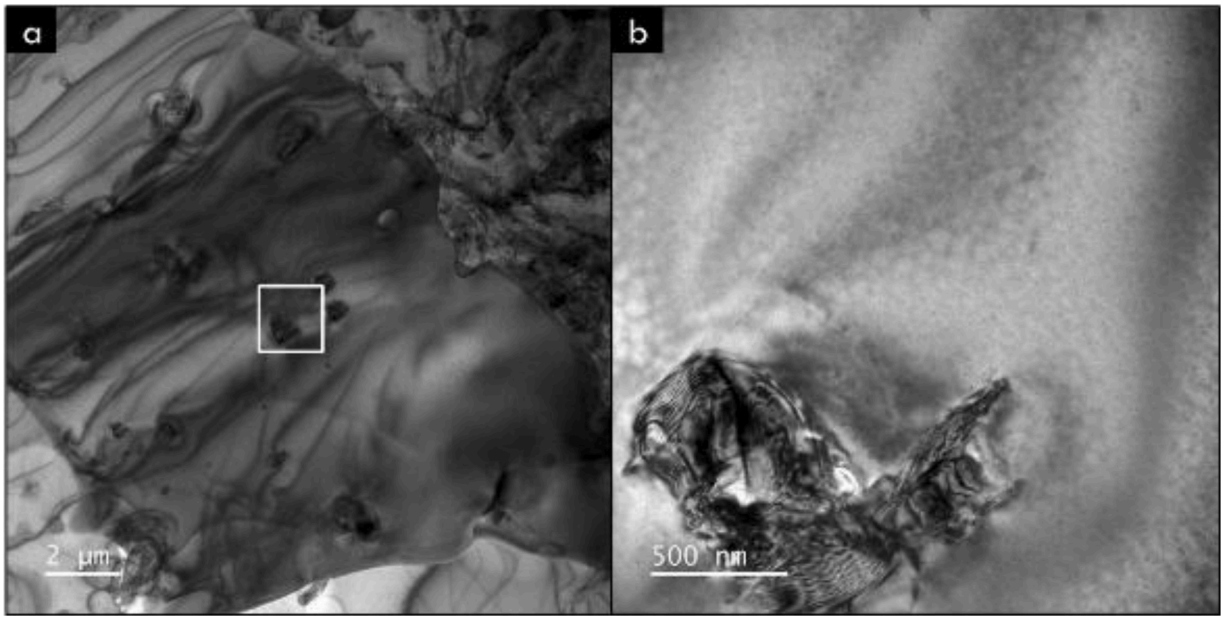

Fig. 3. BF TEM images of the as-recieved CP-Ti: a- An image of an α-phase grain containing precipitates, b- A magnified image of the precipitate highlighted in a.

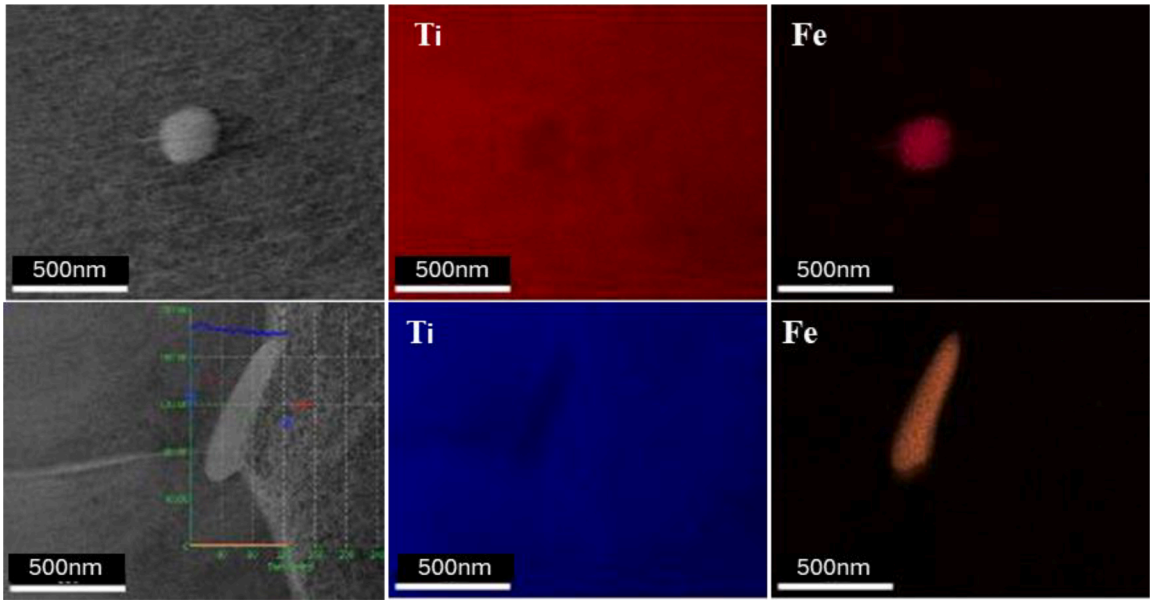

Fig. 4. TEM EDS analysis revealing Fe-rich precipitates in the studied CP Ti.

Table 1
Summary of the different irradiation conditions, where only the final irradiation dose is reported for the in situ experiments.

	Beam	Energy (MeV)	Range (um)	Se (keV/nm)	Flux (ions. $cm^2.s^{-1)}$	Final fluence (ions. $cm^{-2)}$	T (°C)	Calculated final dose for 100 nm foil thickness (dpa)	Dose rate (dpa/s)
In situ irradiation	^{84}Kr	1	0.4	2.3	3.8×10^{11}	5×10^{15}	30	9.4	8.1×10^{-4}
					3.8×10^{11}	1.7×10^{15}	360	3.2	8.1×10^{-4}
					3.8×10^{11}	2.5×10^{14}	430	0.5	8.1×10^{-4}
Ex situ	^{40}Ar	4	1.8	3.2	2.18×10^{13}	4.8×10^{16}	350	7.6	3.5×10^{-3}
irradiation	^{40}Ar	4	1.8	3.2	1.42×10^{12}	2.5×10^{16}	30	4	2.2×10^{-4}

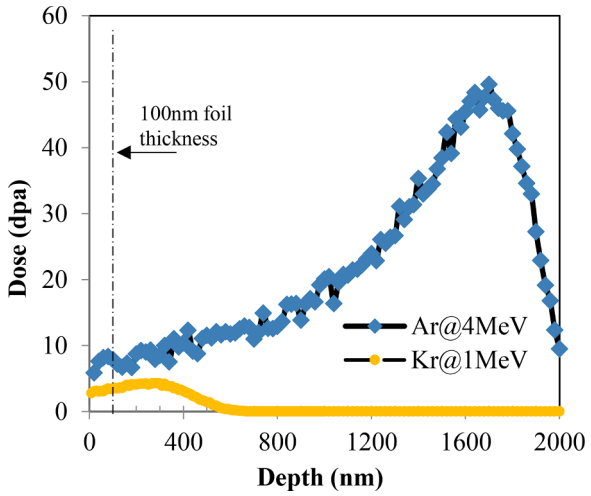

Fig. 5. Simulation of the damage profiles using SRIM software for ^{40}Ar@4MeV and ^{84}Kr@1MeV in Ti for the total ion fluences of 2.5 × 10^{16} ions.cm^{-2} and 1.7 × 10^{15} ions.cm^{-2}, respectively.

ranging in size from 10 to 40 μm, with an average grain size of 30 μm. Precipitates of around 1 μm in diameter were observed as well. The TEM images in Fig. 3 show the initial, as-received grain structure. TEM EDS characterization indicated that the precipitates were Fe-rich, see Fig. 4.

2.4. Irradiation experiments

Details of all the irradiation conditions are provided in Table 1, where only the final irradiation dose is reported for the in situ experiments. The in situ irradiation experiments were performed using a Hitachi H-9000NAR TEM at the Intermediate Voltage Electron Microscopy (IVEM)-Tandem Facility of Argonne National Laboratory. A typical TEM foil thickness of 100 nm allowed for homogeneous irradiation of the entire thickness using a Kr ion beam. The TEM foils were mounted in a double-tilt heating holder and tilted to an angle of 15° to maintain a normal incidence angle of the Kr ion beam to the sample's surface.

The ex situ experiments were performed at Sta. ANA (Stable ion Accelerator for Nuclear Astrophysics) at the University of Notre Dame. Cooling and heating systems were used as required to maintain the desired temperature during the irradiation experiment.

The Displacement per Atom (dpa) calculation was performed using the Kinchin–Pease quick calculation with 5000 ions in the software Stopping and Range of Ions in Materials (SRIM) [27] as recommended in [28]. Using a threshold energy of 30 eV [29], the dose as a function of irradiation depth was estimated for different ion beam energies, flux and fluences as shown in Table 1. An example of the simulated dose as a function of the irradiation particle energy is provided in Fig. 5. The reported final irradiation dose in Table 1 was estimated as the average dose over the 100 nm depth for a typical TEM foil thickness.

2.5. TEM imaging and counting methods

2.5.1. TEM imaging

Weak beam (WB) and bright-field (BF) techniques were used in this work to image dislocation loops [30]. While full characterization by tilting to multiple g vectors was not performed, the main types of radiation-induced dislocation loops in Ti were investigated: i) <a> type dislocation loops with a Burgers vector $\mathbf{b} = \frac{1}{3}\langle 2\bar{1}\bar{1}0\rangle$ that can be imaged with $\mathbf{g}=01\bar{1}0$ and appear as circular or elliptical defects; and ii) c-component dislocation loops in the basal planes that can be imaged with $\mathbf{g} = 0002$. Under the latter diffraction condition, these c-component loops were imaged edge-on and appeared as linear segments perpendicular to the 0002 g vector. For the same grain, tilting to the $[2\bar{1}\bar{1}0]$ zone axis allowed for the distinction between <a> and c-component loops (see the Supplemental Material section for an example). This approach [12] was chosen because the selected g vectors for imaging each loop type are perpendicular. Under each diffracting condition only one type of these loops is visible, where distinct differences in shape and orientation enabled clear and unequivocal identification. While BF images were mainly used for loop counting, dark field (DF) images were used when necessary to reduce the confusion in distinguishing between hydrides and dislocation loops. An example of an identification of the c-component loops is provided in Fig. 6. Hydrides or precipitates, which were not examined in this work, are more easily identified from DF images and were not included in the counting of the c-component loops for example.

The Supplemental Material section provides further details of the TEM imaging techniques as well as some examples of both <a> type and c-component dislocation loop identification and measurements. The observed length of the loop outline in the BF images was referred to as observed loop length. For the irradiation experiments performed at elevated temperature, the irradiating beam was stopped at each image acquisition interval and the temperature was not decreased during

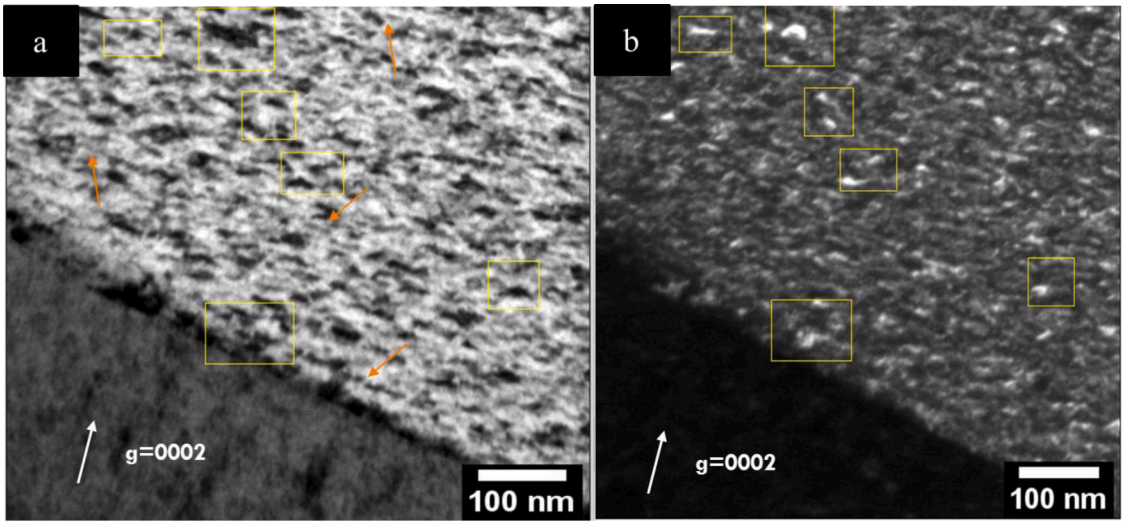

Fig. 6. a) BF and b) DF TEM images in the foil irradiated with 1 MeV Kr at 30°C at a dose of 1.2 dpa. Examples of c-component loops are indicated with orange arrows in a). Features that are not identified as c-component loops are in yellow boxes in both images.

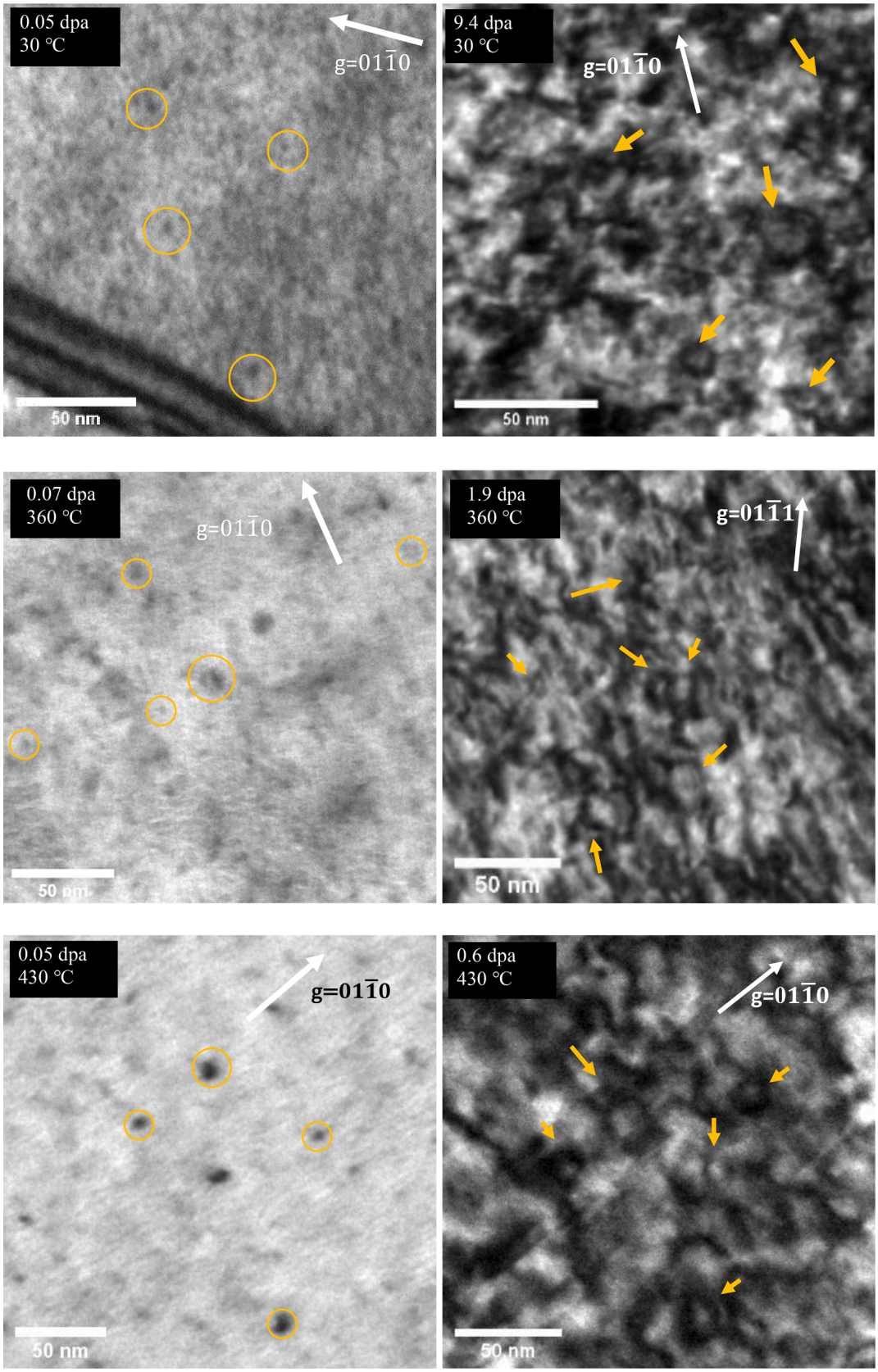

Fig. 7. BF TEM images showing the <a> loops in different TEM foils irradiated with 1 MeV Kr ions at low and high irradiation doses at 30°C, 360°C and 430°C. The <a> loops are indicated with orange circles or arrows.

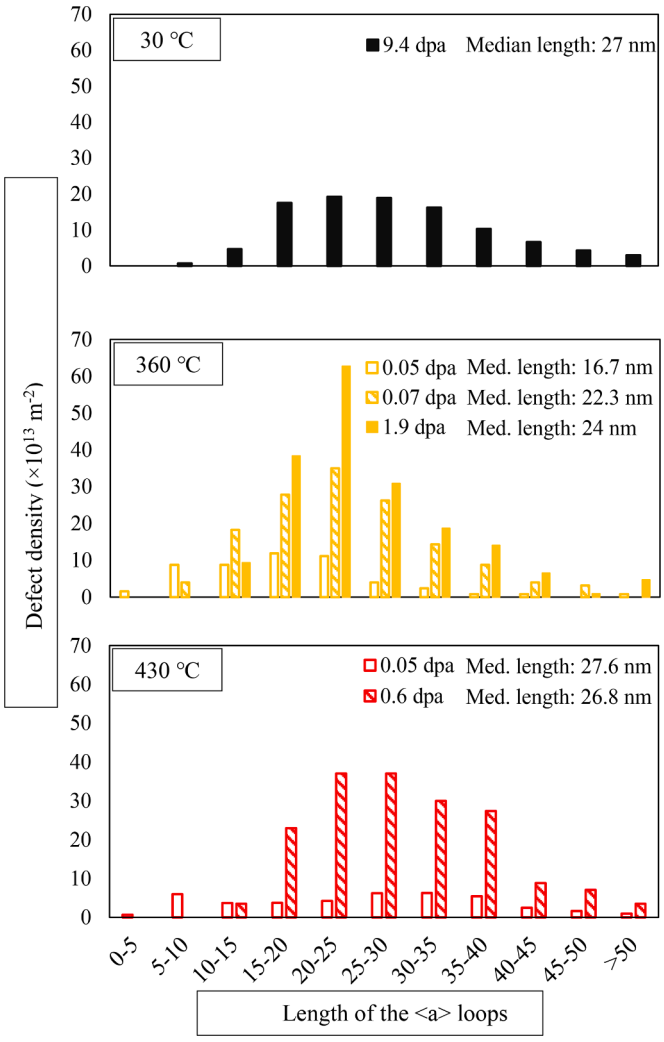

Fig. 8. Distribution of the length of <a> loops in CP Ti irradiated in situ with 1 MeV Kr at: 30°C, 360°C and 430°C.

imaging. An adjustment to the WB conditions was performed to correct for any drift before acquiring the images.

2.5.2. Dislocation density

The dislocation density was calculated from the acquired TEM images at the specified diffraction conditions, and the defect density evolution as a function of irradiation dose was determined in the same volume for each sample. The details of the loop identification and counting methods are included in the Supplemental Material section.

Three different methods were used to represent the dislocation densities: (i) Area dislocation number density**:** This is a measure of the number of dislocation loops (<a> or c-component) in the imaged area; (ii) Dislocation number density**:** This is a measure of the number of dislocation loops (<a> or c-component) in a unit volume (Area × foil thickness); (iii) Linear area dislocation density**:** This additional density was used for c-component loops as their wavy character, especially at high irradiation doses, can make it difficult to determine individual loop length. It is a measure of the sum of the length of the specific dislocation loop types in a unit area**.**

3. Results

3.1. Observation of <a> dislocation loops

3.1.1. In situ observation of <a> dislocation loops

The nucleation habit plane of the prismatic <a> dislocation loops formed during in situ TEM irradiation with 1 MeV Kr ions, regardless of temperature and dose, was {1120}, with Burgers vector $\mathbf{b} = \frac{1}{3}\langle 2\bar{1}\bar{1}0\rangle$ [7]. At low doses between 0.05-0.07 dpa at 25, 350 and 430°C, <a> loops, appearing as black dots in BF images, were homogeneously distributed throughout the grains, as shown in Fig. 7. For higher doses, the <a> loops exhibited a more elliptical shape and a larger size, as illustrated in Fig. 7. High densities of defect clusters were observed in the foil irradiated at 360 and 430°C, (see Fig. 7).

The distributions of the observed length or perimeter of <a> loops in the investigated samples are illustrated in Fig. 8. For samples irradiated at 30°C (see Fig. 7), <a> loops were observed at 0.05 dpa and the average length of the loops was 9 nm. Since the loops were too small for precise length quantification, the area number density of these defects was counted using brightness maxima in the image processing tool Fiji [31]. All the distributions of the length of the loops were slightly right skewed. For each irradiation temperature, as the dose increased, the skewness moved further right. As a result, the median values of the <a> loop length increased as a function of dose for each irradiation temperature (see Fig. 8). The area under the curve also increased as the dose increased, which suggests a cumulative increase in total defect number density.

3.1.2. Ex situ observation of <a> dislocation loops

For the samples irradiated ex situ with 4 MeV Ar ions, the irradiation dose corresponds to the dose at the preserved surface of the sample.

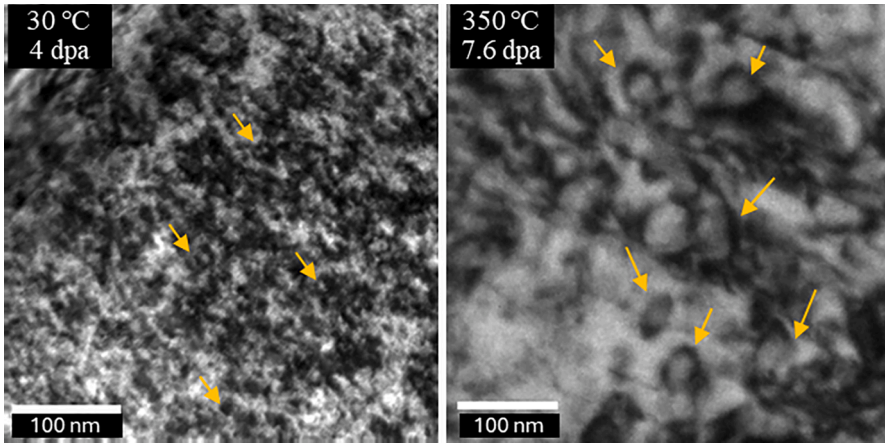

Fig. 9. BF TEM images with $\mathbf{g} = 01\bar{1}0$ showing the CP Ti sample irradiated ex situ with 4 MeV Ar ions at the indicated surface doses and temperatures. The orange arrows indicate some of the <a> loops, which were significantly larger at both higher temperature and dose.

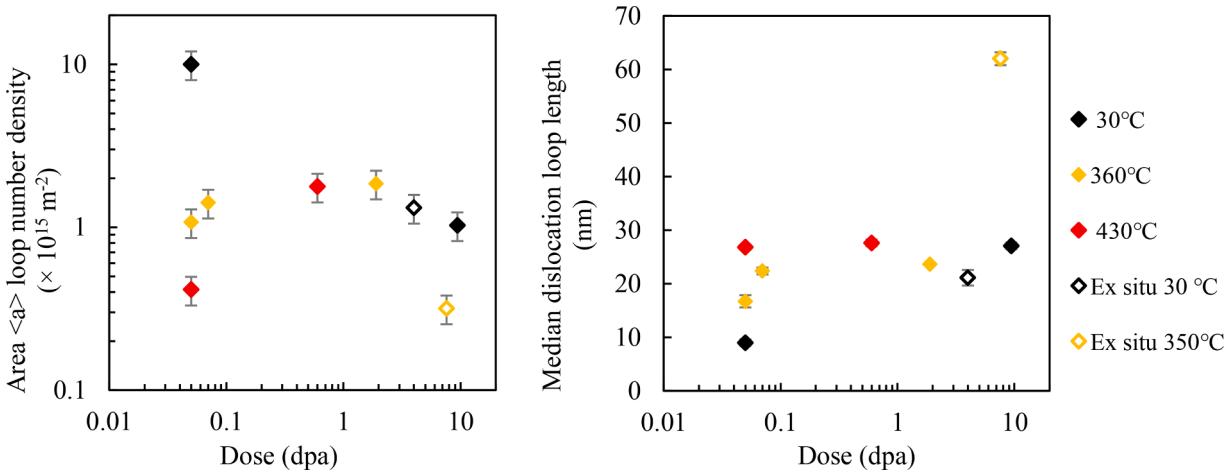

Fig. 10. Quantification of <a> dislocation loops in CP Ti irradiated in situ with 1 MeV Kr and ex situ with 4 MeV Ar at different temperatures as a function of dose.

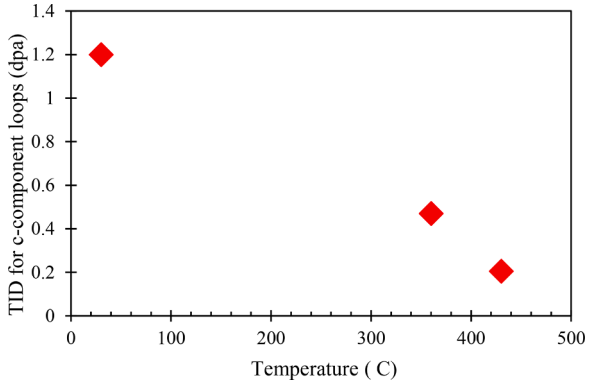

Fig. 11. Threshold incubation dose (TID) for c-component loops as a function of temperature.

These were 4 dpa and 7.6 dpa for the irradiation temperatures of 30°C and 350°C, respectively. These samples exhibited both <a> dislocation lines and <a> loops, as indicated by orange arrows in Fig. 9. The size of the loops was larger in the sample irradiated at 350°C (Fig. 9).

3.1.3. Effect of dose and temperature

The area <a> loop number density[2], and their median length as a function of dose for CP Ti irradiated at different temperatures, are presented in Fig. 10. For the sample irradiated at 30°C, the <a> loop area number density decreased from ~10^{16} m^{-2} to 10^{15} m^{-2} with increasing dose. This significant decrease in number density per unit area corresponded with a significant increase in the median loop size from 9 nm to 27 nm. In contrast, for the sample irradiated at 360°C, the area number density increased slightly between the doses of 0.05 to 0.07 dpa, while the median loop size went from 16 nm to 22 nm. With the higher dose of 1.9 dpa, the <a> loop area number density appeared to saturate at a value of 1.8 × 10^{15} m^{-2}. At 430°C, the <a> loop area number density increased significantly, from 4 × 10^{14} m^{-2} to 1.8 × 10^{15} m^{-2}, with increasing dose, but the loop size did not increase significantly. At the low irradiation dose, the sample irradiated at the lowest temperature had a much higher defect density and a smaller loop size. As the temperature increased, the defect number density decreased, and the loop size increased.

3.2. Observations of c-component dislocation loops

3.2.1. In situ observations of c-component loops

The threshold incubation dose (TID) of c-component loops in CP Ti was determined at different temperatures. The TID for c-component loops as a function of irradiation temperature is plotted in Fig. 11, where the TID decreased from 1.2 dpa to 0.2 dpa as the irradiation temperatures increased from 30°C to 430°C. Although these TID values observed in CP Ti are significantly lower than reported for pure Zr, the decrease of the TID as a function of dose is consistent with other studies [32]. The difference between c-component loop nucleation in Zr and Ti alloys will be discussed later.

Figs 12–14 illustrate the observed increase in c-component loop nucleation as a function of increasing dose at 30, 360 and 430°C. Dislocation denuded zones[3] at the grain boundary were not observed in irradiated CP Ti for any of the temperatures examined. In fact, c-component loops were observed at a distance less than 10 nm from the grain boundary in all samples. Fig. 15 shows an example of the observed coalescence of smaller neighboring loops to form longer features that were identifiable as c-component loops.

The distributions of the length of the c-component loops in foils irradiated in situ at 30°C, 360°C and 430°C, at different doses, are shown in Fig. 16. All the distributions are right-skewed. As the dose increases, the right-skewed distributions move further to the right. As a result, the median values of the c-component loop length increase as a function of dose for each temperature. For the irradiation temperature of 360°C and between the doses of 0.9 and 1.9 dpa, the size of previously nucleated loops increased while a few new loops formed (see Fig. 16).

A similar trend was observed for the sample irradiated at 430°C. The increase in c-component loops length above 50 nm with increased dose was significant (see Fig. 16). At the final irradiation dose of 0.6 dpa, both small (between 5 and 10 nm) and large (above 50 nm) loops were present in the foils and as shown in Fig. 16 for 430°C, and red arrows indicated the two highest loop diameter peaks.

3.2.2. Ex situ observation of c-component loops

TEM foils made from CP Ti samples irradiated ex situ with 4 MeV Ar ion beams at 30°C and 350°C were also examined. As the irradiation temperature increased, the c-component loop length increased, see Fig. 17.

3.2.3. Effect of dose and temperature

To better understand the effect of the dose and temperature on the

[2] The area loop number density is defined as the number of specific dislocation loop types (<a> or c-component) in a unit area [m^{-2}].

[3] Dislocation-free zone observed in the case of irradiated Zr alloys [66].

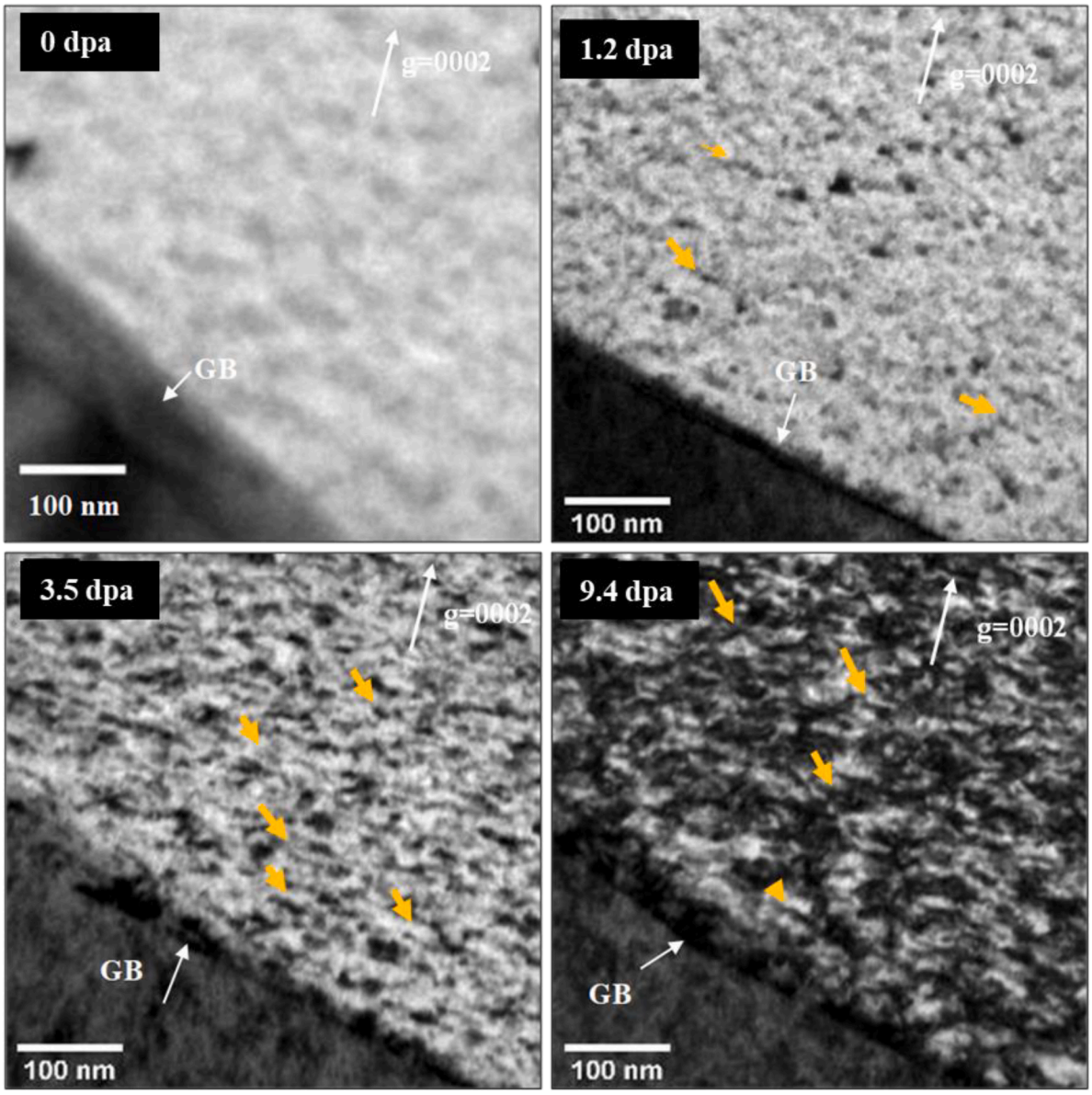

Fig. 12. BF TEM images showing the c-component loop evolution and growth in samples irradiated with 1 MeV Kr at 30°C at increasing doses in the same area. Orange arrows point to some of the observed c-component loops in each micrograph. The grain boundary (GB) is indicated with a white arrow in each image.

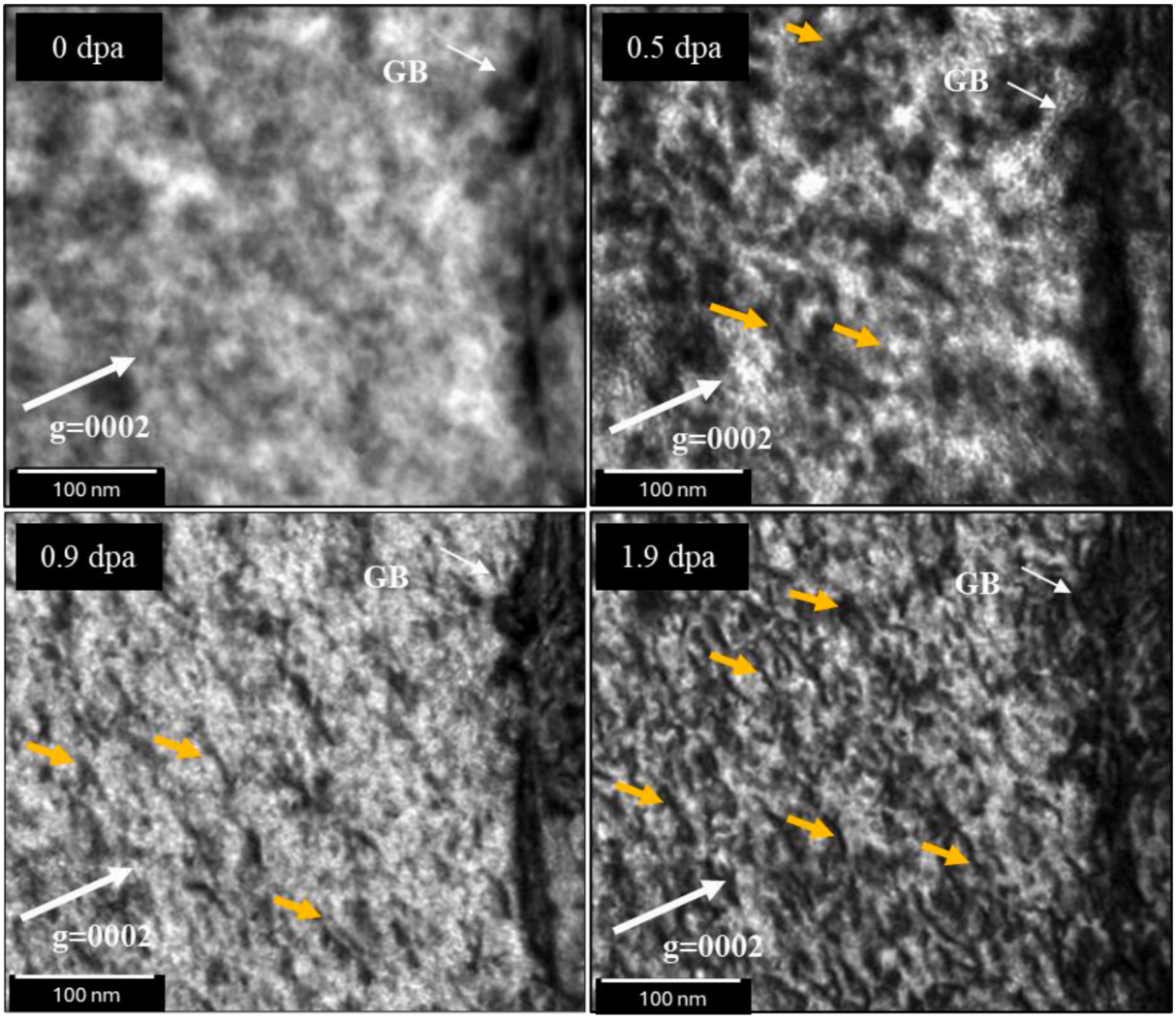

Fig. 13. BF TEM images showing the c-component loop evolution and growth in samples irradiated with 1 MeV Kr at 360°C at increasing doses in the same area. The grain boundary (GB) is indicated with a white arrow in each image. Orange arrows indicate some of the observed c-component loops.

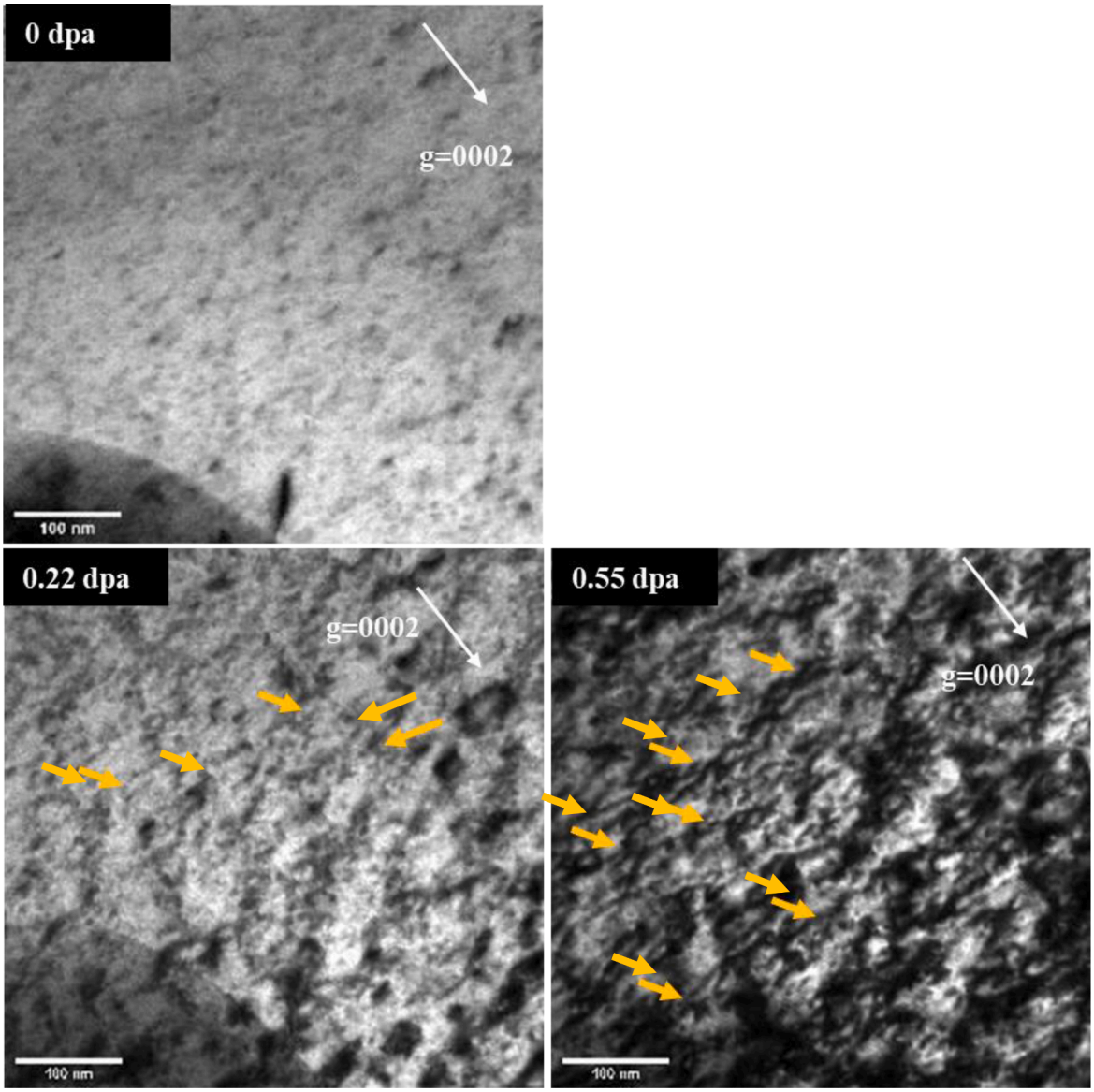

Fig. 14. BF TEM images showing the c-component loop evolution and growth in samples irradiated with 1 MeV Kr at 430°C at increasing doses in the same area. Orange arrows indicate some of the observed c-component loops.

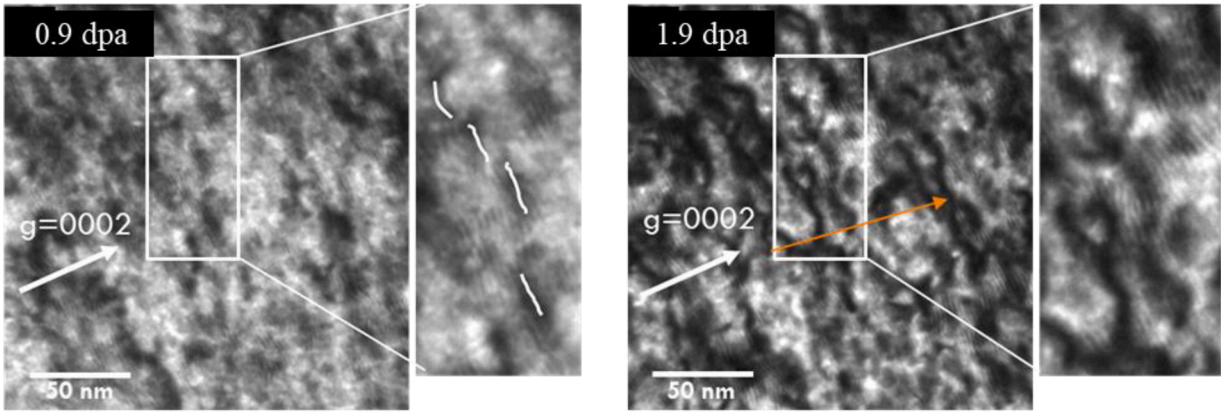

Fig. 15. BF TEM images showing coalescence of smaller neighboring loops to form longer strings, identifiable as c-component type loops, in foils irradiated with 1 MeV Kr at 360°C at increasing doses.

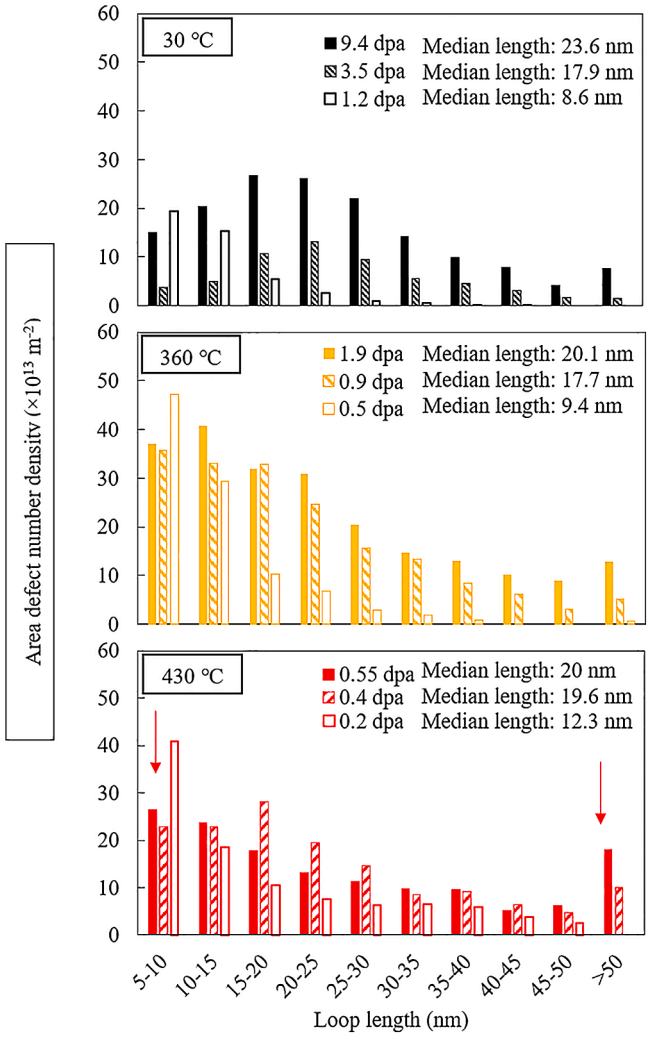

Fig. 16. Distributions of the observed length of c-component loops in samples irradiated in situ with 1 MeV Kr at 30°C, 360°C and 430°C. Red arrows in the 430°C distribution point to the two peak densities in the sample irradiated up to a dose of 0.55 dpa.

evolution of c-component loops in CP Ti at different temperatures and doses, defect number densities, linear densities, and median values of the c-component loop length were plotted (see Figs. 18 and 19). For in situ irradiations, the defect number densities for the sample irradiated at 30°C were the lowest observed and they increased with increasing dose. A similar trend of increasing defect number densities with increasing dose was observed for the 430°C data, but at 360°C, a shallower increase in defect densities was observed with increasing dose. Assessment using the defect linear defect density in Fig. 19 provides a more distinct separation of the data trends. Additional higher dose data are needed at 30 and 430°C to verify whether the c-component loop evolution saturates at lower than 0.6 dpa, at 430°C, and to determine if the rate of increase of the defect densities at lower doses is similar to that at the other two temperatures.

Ex situ irradiation at 30°C resulted in a higher density of shorter c-component loops than during in situ irradiation at a similar dose (4 dpa). Consequently, the defect linear density was consistent with the trend observed for samples irradiated in situ (Fig. 19). On the other hand, the samples irradiated ex situ at 350°C and for a dose of 7.6 dpa exhibited a significantly lower defect number density and a higher median loop length (27 nm). It should be noted that 20% of counted loops were larger than 50 nm.

4. Discussion

4.1. Evolution of <a> loops

For hcp metals, prismatic <a> dislocation loops have been correlated with an increase in hardness and reduction in elongation-to-failure [5]. A high density of small dislocation loops, constituting a hardened microstructure [11], was observed in the investigated grains at lower irradiation doses (Fig. 9). These small defects were also observed in Zr [32] and are identified as <a> dislocation loops formed by the collapse of vacancy and interstitial clusters [7]. As the irradiation dose increased, the loop size increased, as observed for all irradiation temperatures (see Fig. 10). Similar to the case of Zr [32], loop growth is thought to occur as a result of loop calescence, i.e. the absorption of smaller loops into larger loops [12,13]. Although this coalescence was not observed experimentally for <a>loops in this work, Fig. 8 shows that small new loops were continuously nucleated while the loop number density decreased especially for doses higher than 1 dpa, consistent with Fig. 10. The final damage structure at 360 and 430°C included dislocation loops and clusters (see Fig. 9).

The measured defect number density of the <a> dislocation loops,

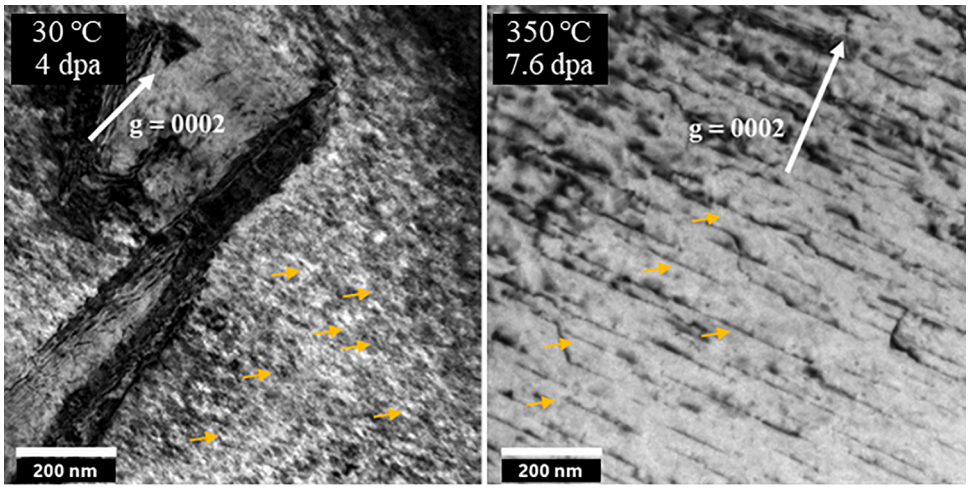

Fig. 17. BF TEM images showing evolution of c-component loops in CP Ti samples irradiated ex situ with 4 MeV Ar ions (**g** = 0002) at 30°C and 350°C. Orange arrows indicate some of the observed c-component loops.

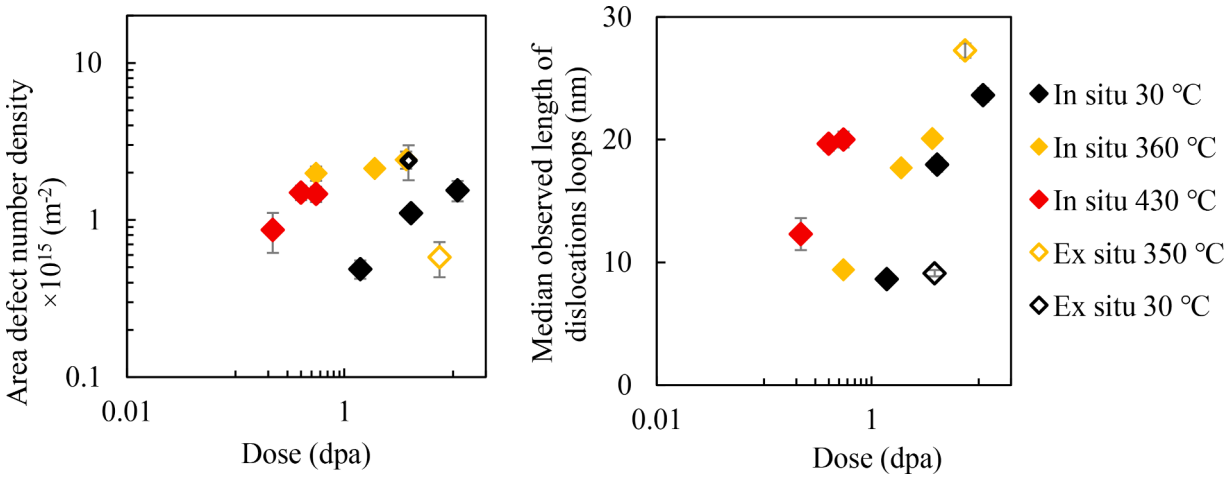

Fig. 18. The number area density and size of observed c-component loops increased with dose and temperature.

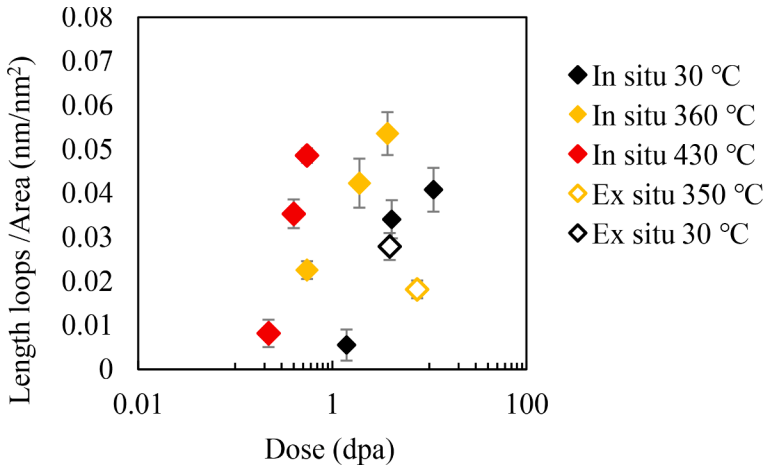

Fig. 19. C-component loop defect linear density increased with both increasing dose and temperature.

and their equivalent circular diameter (ECD)[4], are compared to the results of ion [11] and proton [9] irradiation in Fig. 20. As expected, both temperature and dose dependencies were observed for all samples. High defect densities and smaller defect sizes were reported at a low temperature in the samples irradiated with 1 MeV Kr and 590 MeV protons [9]. The defect density decreased for higher temperatures while the <a> loop size increased.

Since the radiation induced defect structure is dependent on the irradiating particles, temperature, dose, and the dose rate, the effect of the latter on the evolution of <a> dislocation loops in Ti was investigated in Fig. 20 and the corresponding Table 2. The comparison between ex situ and in situ irradiations in the current work shows that the dose rate effect was minimal at low temperature while it was more significant at 350°C. Ex situ irradiation was performed at a higher dose rate than in situ irradiations and resulted in a lower <a> loop density. This is consistent with observations in a similar CP Ti [11], as well as lower defect densities after proton irradiations. At higher temperatures, defect densities resulting from proton irradiations [9] at lower does rates were higher than those for ion irradiation in results from both the current work and in [11]. At higher temperatures, higher dose rates resulted in higher defect densities due to the enhanced mobility of point defects and their recombination [32].

4.2. Evolution of c-component loops and TID

Radiation-induced growth in hcp metals is enhanced for samples containing c-component loops [33], which prompted extensive studies of c-component loop nucleation in Zr and Zr alloys [33–36]. The diffusional anisotropy difference (DAD) model [37], where single interstitial atoms (SIA) are more mobile on the basal plane and vacancies have anisotropic diffusion, provides an explanation of the growth of c-component loops [36]. As a result of DAD, grain boundaries and dislocations parallel to the c-component axis absorb most interstitial atoms formed after irradiation leading to elongation along the <a> axis and contraction along the c-component axis [38]. Investigations of c-component loops in Ti are limited [7,12,19] and the current study is the first (to the authors' knowledge) to investigate their evolution in situ at different temperatures and doses. The stability and evolution of c-component loops depend on the presence of impurities, the temperature, the dose and their TID [5,24,32].

Similar to Zr alloys [32,39], the current work shows that

[4] ECD is calculated using the area (A) and the perimeter (P) of the <a> dislocation loop: $ECD = \sqrt{\frac{4A}{\pi} + \left(\frac{P}{\pi}\right)^2}$

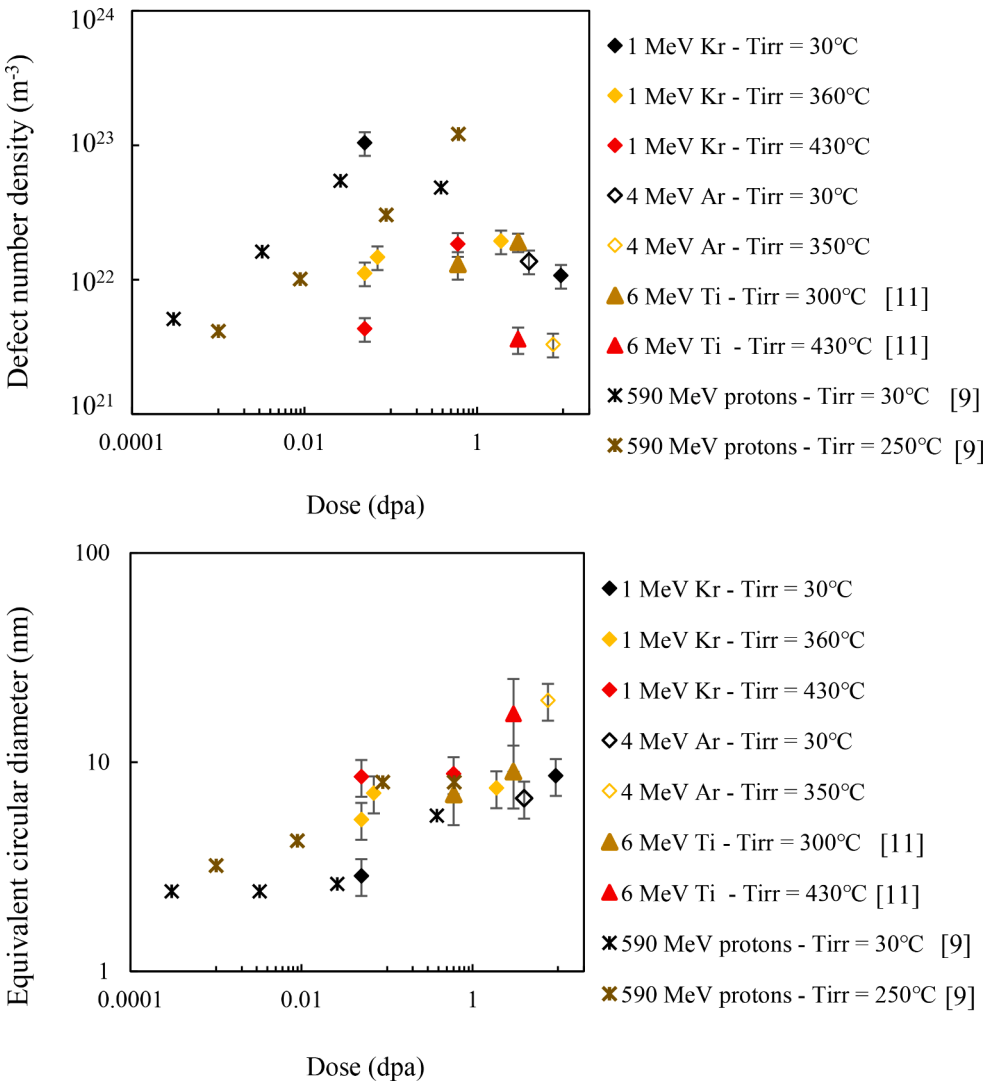

Fig. 20. Defect number density and the equivalent circular diameter of <a> loops in CP Ti verses dose comparing the current work (diamond symbols) with prior research [9,11]. A high density of small loops is observed at low temperature. At higher temperature, proton irradiation at lower dose rates resulted in higher defect densities with comparable loop diameters. Overall, the equivalent circular diameter of <a> loops increased with increasing dose.

Table 2
Irradiation conditions corresponding to the data plotted in Fig. 20

	Beam	Energy (MeV)	T (°C)	Calculated dose for 100 nm foil thickness (dpa)	Dose rate (dpa/s)
In situ irradiation	^{84}Kr	1	30	9.4	8.1×10^{-4}
			360	3.2	8.1×10^{-4}
			430	0.5	8.1×10^{-4}
Ex situ irradiation	^{40}Ar	4	350	7.6	3.5×10^{-3}
			30	4	2.2×10^{-4}
Ref [11]	Ti2+	6	300	3	2.2×10^{-4}
	Ti2+	6	430	0.6	2.3×10^{-4}
Ref [9]	Proton	590	250	0.61	10^{-7}
	Proton	590	30	0.4	10^{-7}

c-component loops occur after reaching a TID and that temperature is one of the main factors assisting the formation of these loops. The TID in the current work was reported in the same way in [32] and is defined as the dose at which c-component loops were unambiguously identified in BF TEM images. In CP Ti, c-component loops nucleated more easily in samples irradiated at higher temperatures, as shown in Fig. 21. While previous observations of c-component loops were made at the low dose of 0.6 dpa [12], the actual TID was much lower in the currently investigated CP-Ti, especially compared to Excel Zr alloy [32]. The migration and formation energies of vacancies and interstitials in Zr are higher than those of Ti [35], which may explain the lower doses at which c-component loop were observed in the current work. Other factors

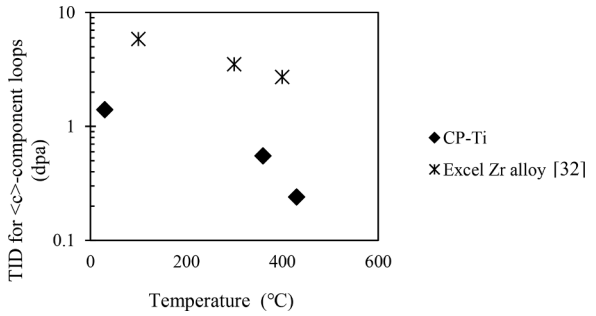

Fig. 21. The TID for c-component loops in CP Ti from the current work is lower than that for Excel Zr alloy [32] irradiated in situ with 1 MeV Kr ions at the IVEM facility.

assisting the formation of c-component loops are alloying or impurity elements, especially Fe [24] and hydrogen [40]. Radiation induced dissolution of the Fe-rich precipitates, present in the studied CP-Ti (Fig. 4), or hydrides that formed during TEM sample preparation could contribute to the early c-component loop growth. Compared to c-component loops in Zr [24], the observed edge-on c-component loops were not straight. Their curved or wavy appearance was enhanced at higher temperatures (see Figs. 12–14). This phenomenon could be explained by dislocation loop climbing as a result of vacancy absorption, which is enhanced at higher temperatures [5,11].

The c-component loop growth mechanism in CP-Ti is similar to Zr [11,12,32], relying on loop calescence as shown in Fig. 15. A comparison between the evolution of c-component loops in CP Ti and Zr [24] during irradiation with 1 MeV Kr ions is presented in Fig. 22. Although the area defect number densities were comparable, the average lengths of the observed c- component loops are higher in Zr than in CP Ti. Radiation-induced swelling is therefore expected to be higher in Zr. Data on the swelling of Ti was not available to confirm this hypothesis.

5. Conclusions

This study explored the impact of heavy ion radiation damage on CP Ti and provided a systematic quantitative analysis of radiation-induced defects that can be used to model the changes to its mechanical properties. The observations of the nucleation and growth of <a> and c-component loops led to the following findings:

(1) Observation and quantification of prismatic <a> dislocation loops during in situ TEM irradiations with 1 MeV Kr ions at 30°C, 360°C and 430°C were reported. At doses between 0.05 dpa and 0.06 dpa, the <a> loops appear to be homogeneously distributed throughout the grains. As the irradiation dose increased, these loops unfaulted and their size in the TEM foils increased at all the investigated irradiation temperatures. Dislocation clusters were only observed in the final damage structure at 430°C. At this temperature, the average loop diameters were ~8.5 nm.

(2) C-component loops were only observed after reaching a TID. These loops nucleated at much lower doses in CP Ti than for Zr. TID decreased with increasing temperature for doses of 1.4 dpa, 0.55 dpa, and 0.24 dpa, and for irradiation temperatures of 30°C, 360°C and 430°C, respectively. The migration and formation energies of vacancies and interstitials in Zr are higher than those of Ti and this could explain these lower TID values in addition to thermal and radiation-induced dissolution of Fe-rich precipitates and hydrides.

(3) Loop growth occurred as a result of loop coalescence or the absorption of smaller loops into larger loops was observed for c-component loops. Alongside the already formed loops, small new defects were also present. The size of c-component loops and their defect number densities increased linearly at 30°C and 360°C without showing signs of saturation up to a dose of 9.4 and 1.9 dpa respectively. The foil irradiated at 430°C seemed to reach a maximum loop size and loop density at the low dose of 0.6 dpa.

CRediT authorship contribution statement

A. Amroussia: Writing – original draft, Writing – review & editing, Methodology, Investigation, Formal analysis, Data curation, Funding acquisition, Conceptualization. **C.J. Boehlert:** Writing – review & editing, Supervision, Resources, Project administration, Funding acquisition, Data curation, Conceptualization. **F. Pellemoine:** Writing – review & editing, Supervision, Resources, Project administration, Funding acquisition, Data curation, Conceptualization. **D. Grummon:** Writing – review & editing, Supervision. **W. Mittig:** Supervision, Conceptualization. **T.R. Bieler:** Writing – review & editing, Supervision. **M. Li:** Investigation, Data curation. **W.-Y. Chen:** Investigation, Data curation.

Declaration of competing interest

The authors declare that they have no known competing financial interests or personal relationships that could have appeared to influence the work reported in this paper.

Data availability

Data will be made available on request.

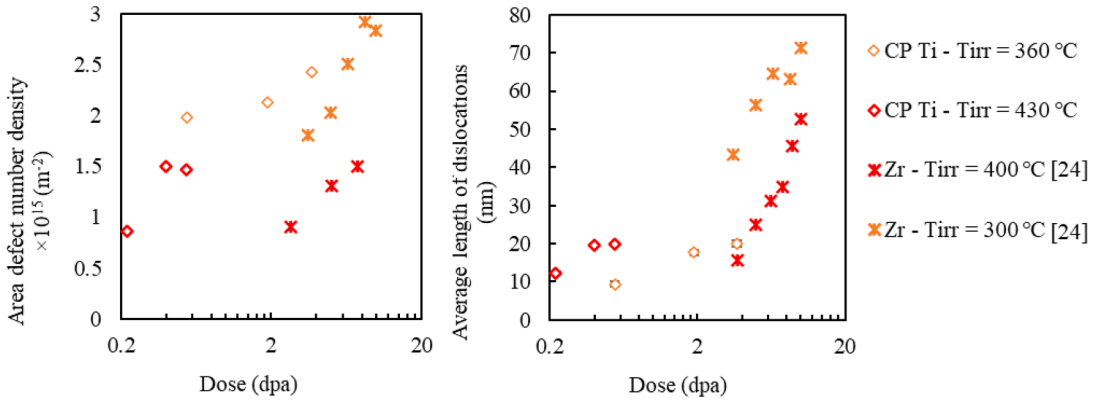

Fig. 22. Under 1 MeV Kr ion irradiation, c-component dislocation loops in CP Ti (current work) exhibited a higher area defect number density than in Zr [24] at lower doses, but their length increased at a lower rate in CP Ti.

Acknowledgments

This work was partially supported by the U.S. Department of Energy, Office of Science, under Cooperative Agreement DE-SC0000661, and was also supported by Michigan State University under the Strategic Partnership Grant “FRIB - Materials in Extreme Environments”. The in situ TEM irradiations at the Intermediate Voltage Electron Microscopy (IVEM)-Tandem Facility, Argonne National Laboratory, IL, USA, and post-irradiation characterization at Oak Ridge National Laboratory (ORNL), TN, USA were supported by the U.S. Department of Energy, Office of Nuclear Energy under DOE Idaho Operations Office Contract DE-AC07- 051D14517 as part of a Nuclear Science User Facilities experiment. Work performed at the Center for Nanoscale Materials (CNM), Argonne National Laboratory, IL, USA, an Office of Science user facility, was supported by the U.S. Department of Energy under Contract No. DE-AC02-06CH11357.

Supplementary materials

Supplementary material associated with this article can be found, in the online version, at doi:10.1016/j.jnucmat.2024.155105.

References

[1] J.W. Davis, M.A. Ulrickson, R.A. Causey, Use of titanium in fusion components, J. Nucl. Mater. 212 (1994) 813–817.
[2] T. Ishida, E. Wakai, S. Makimura, P.G. Hurh, K. Ammigan, A.M. Casella, D. J. Edwards, D.J. Senor, C.J. Densham, M. Fitton, J. Bennett, D. Kim, N. Simos, M. Calviani, C. Torregrosa Martin, Radiation Damage Studies on Titanium Alloys as High Intensity Proton Accelerator Beam Window Materials, in: Proc. 14th Int. Workshop Spallation Mater. Technol., Journal of the Physical Society of Japan, Fukushima, Japan, 2020, https://doi.org/10.7566/JPSCP.28.041001.
[3] A. Amroussia, M. Avilov, C.J. Boehlert, F. Durantel, C. Grygiel, W. Mittig, I. Monnet, F. Pellemoine, Swift heavy ion irradiation damage in Ti–6Al–4V and Ti–6Al–4V–1B: Study of the microstructure and mechanical properties, Nucl. Instrum. Methods Phys. Res. Sect. B Beam Interact. Mater. At 365, Part B (2015) 515–521, https://doi.org/10.1016/j.nimb.2015.09.029.
[4] M. Avilov, A. Aaron, A. Amroussia, W. Bergez, C. Boehlert, T. Burgess, A. Carroll, C. Colin, F. Durantel, P. Ferrante, T. Fourmeau, V. Graves, C. Grygiel, J. Kramer, W. Mittig, I. Monnet, H. Patel, F. Pellemoine, R. Ronningen, M. Schein, Thermal, mechanical and fluid flow aspects of the high power beam dump for FRIB, Nucl. Instrum. Methods Phys. Res. Sect. B Beam Interact. Mater. At. 376 (2016) 24–27, https://doi.org/10.1016/j.nimb.2016.02.068.
[5] M. Griffiths, Evolution of microstructure in hcp metals during irradiation, J. Nucl. Mater. 205 (1993) 225–241.
[6] S. Tähtinen, P. Moilanen, B.N. Singh, Effect of displacement dose and irradiation temperature on tensile and fracture toughness properties of titanium alloys, J. Nucl. Mater. 367–370 (2007) 627–632, https://doi.org/10.1016/j.jnucmat.2007.03.042.
[7] M. Griffiths, D Faulkner, R.C Styles, NEUTRON DAMAGE IN a-TITANIUM, J. Nucl. Mater. 119 (1983) 189–207.
[8] P. Marmy, T. Leguey, Impact of irradiation on the tensile and fatigue properties of two titanium alloys, J. Nucl. Mater. 296 (2001) 155–164.
[9] T. Leguey, N. Baluc, R. Schäublin, M. Victoria, Temperature dependence of irradiation effects in pure titanium, Philos. Mag. 85 (2005) 689–695, https://doi.org/10.1080/14786430412331319992.
[10] T. Leguey, N. Baluc, R. Schäublin, M. Victoria, Structure–mechanics relationships in proton irradiated pure titanium, J. Nucl. Mater. 307–311 (2002) 696–700, https://doi.org/10.1016/S0022-3115(02)01190-X.
[11] E. Jouanny, S. Doriot, J. Malaplate, M. Dehmas, L. Allais, M.L. Thuaut, T. Millot, Evolution of defects in titanium grade 2 under Ti^{2+} ion irradiation, J. Microsc. 265 (2017) 275–286, https://doi.org/10.1111/jmi.12499.
[12] S. Doriot, E. Jouanny, J. Malaplate, F. Dalle, L. Allais, T. Millot, M. Descoins, D. Mangelinck, M. Dehmas, Evolution of defects in Ti6-4 under Ti2+ ion irradiation: Focus on radiation-induced precipitates, J. Nucl. Mater. 511 (2018) 264–276, https://doi.org/10.1016/j.jnucmat.2018.09.027.
[13] E. Jouanny, Etude de l’évolution microstructurale sous irradiation aux ions Ti2+ de deux alliages de titane. Lien avec les propriétés mécaniques, PhD Thesis, Universite de Lorraine, 2017.
[14] P. Wilkes, G.L. Kulcinski, Heavy ion irradiation of a Ti-6Al-4V alloy, J. Nucl. Mater. 78 (1978) 427–430.
[15] H. Föll, M. Wilkens, A simple method for the analysis of dislocation loops by means of the inside-outside contrast on transmission electron micrographs, Phys. Status Solidi A 31 (1975) 519–524, https://doi.org/10.1002/pssa.2210310223.
[16] W. Frank, Intrinsic point defects in hexagonal close-packed metals, J. Nucl. Mater. 159 (1988) 122–148, https://doi.org/10.1016/0022-3115(88)90090-6.
[17] R.W. Gilbert, K. Farrell, C.E. Coleman, Damage structure in zirconium alloys neutron irradiated at 573 to 923 k, J. Nucl. Mater. 84 (1979) 137–148, https://doi.org/10.1016/0022-3115(79)90157-0.
[18] C.H. Woo, Defect accumulation behaviour in hcp metals and alloys, J. Nucl. Mater. 276 (2000) 90–103, https://doi.org/10.1016/S0022-3115(99)00172-5.
[19] M. Griffiths, Microstructure evolution in h.c.p. metals during irradiation, Philos. Mag. A 63 (1991) 835–847, https://doi.org/10.1080/01418619108213917.
[20] A. Dutta Gupta, P. Mukherjee, N. Gayathri, P. Bhattacharyya, M. Bhattacharya, A. Sarkar, S. Sen, M.K. Mitra, Proton irradiation studies on pure Ti and Ti-6Al-4V, Nucl. Instrum. Methods Phys. Res. Sect. B Beam Interact. Mater. At. 387 (2016) 63–72, https://doi.org/10.1016/j.nimb.2016.09.010.
[21] F. Onimus, L. Dupuy, F. Mompiou, In situ TEM observation of interactions between gliding dislocations and prismatic loops in Zr-ion irradiated zirconium alloys, Prog. Nucl. Energy 57 (2012) 77–85, https://doi.org/10.1016/j.pnucene.2011.10.005.
[22] M. Li, M.A. Kirk, P.M. Baldo, E.A. Ryan, TEM with in situ Ion Irradiation of Nuclear Materials: The IVEM-Tandem User Facility, Microsc. Microanal 21 (2015) 437–438, https://doi.org/10.1017/S1431927615002986.
[23] M. Li, M.A. Kirk, P.M. Baldo, D. Xu, B.D. Wirth, Study of defect evolution by TEM with *in situ* ion irradiation and coordinated modeling, Philos. Mag. 92 (2012) 2048–2078, https://doi.org/10.1080/14786435.2012.662601.
[24] Y. Idrees, Z. Yao, M.A. Kirk, M.R. Daymond, In situ study of defect accumulation in zirconium under heavy ion irradiation, J. Nucl. Mater. 433 (2013) 95–107, https://doi.org/10.1016/j.jnucmat.2012.09.014.
[25] Hongmei Li, Analysis of the deformation behavior of the hexagonal close-packed alpha phase in titanium and titanium alloys, Michigan State University, 2013.
[26] E04 Committee, Test Methods for Determining Average Grain Size, ASTM International, n.d. https://doi.org/10.1520/E0112-96R04.
[27] J.F. Ziegler, M.D. Ziegler, J.P. Biersack, SRIM – The stopping and range of ions in matter (2010), Nucl. Instrum. Methods Phys. Res. Sect. B Beam Interact. Mater. At. 268 (2010) 1818–1823, https://doi.org/10.1016/j.nimb.2010.02.091.
[28] R.E. Stoller, M.B. Toloczko, G.S. Was, A.G. Certain, S. Dwaraknath, F.A. Garner, On the use of SRIM for computing radiation damage exposure, Nucl. Instrum. Methods Phys. Res. Sect. B Beam Interact. Mater. At. 310 (2013) 75–80, https://doi.org/10.1016/j.nimb.2013.05.008.
[29] Standard Practice for Neutron Radiation Damage Simulation by Charged-Particle Irradiation, in: E521-Annu. Book ASTM Stand., American Society for Testing and Materials, Philadelphia, PA, n.d.
[30] M.L. Jenkins, Characterisation of radiation-damage microstructures by TEM, J. Nucl. Mater. 216 (1994) 124–156, https://doi.org/10.1016/0022-3115(94)90010-8.
[31] J. Schindelin, I. Arganda-Carreras, E. Frise, V. Kaynig, M. Longair, T. Pietzsch, S. Preibisch, C. Rueden, S. Saalfeld, B. Schmid, J.-Y. Tinevez, D.J. White, V. Hartenstein, K. Eliceiri, P. Tomancak, A. Cardona, Fiji: an open-source platform for biological-image analysis, Nat. Methods 9 (2012) 676, https://doi.org/10.1038/nmeth.2019.
[32] Y. Idrees, Microstructural evolution in Zr and Zr alloy Excel under ion irradiation., Library and Archives Canada = Bibliothèque et Archives Canada, 2014.
[33] R.A. Holt, R.W. Gilbert, ⟨c⟩Component dislocations in annealed Zircaloy irradiated at about 570 K, J. Nucl. Mater. 137 (1986) 185–189, https://doi.org/10.1016/0022-3115(86)90218-7.
[34] T.D. Gulden, I.M. Bernstein, Dislocation loops in irradiated zirconium, Philos. Mag. 14 (1966) 1087–1091, https://doi.org/10.1080/14786436608244779.
[35] N. Gharbi, F. Onimus, D. Gilbon, J.-P. Mardon, X. Feaugas, Impact of an applied stress on c-component loops under Zr ion irradiation in recrystallized Zircaloy-4 and M5®, J. Nucl. Mater. 467 (2015) 785–801, https://doi.org/10.1016/j.jnucmat.2015.10.009.
[36] M. Griffiths, A review of microstructure evolution in zirconium alloys during irradiation, J. Nucl. Mater. 159 (1988) 190–218, https://doi.org/10.1016/0022-3115(88)90093-1.
[37] C.H. Woo, Theory of irradiation deformation in non-cubic metals: Effects of anisotropic diffusion, J. Nucl. Mater. 159 (1988) 237–256, https://doi.org/10.1016/0022-3115(88)90096-7.
[38] F. Onimus, J.L. Béchade, 4.01 - Radiation Effects in Zirconium Alloys, in: R.J. M. Konings (Ed.), Compr. Nucl. Mater., Elsevier, Oxford, 2012, pp. 1–31, https://doi.org/10.1016/B978-0-08-056033-5.00064-1.
[39] C. Yan, R. Wang, Y. Wang, X. Wang, G. Bai, Effects of ion irradiation on microstructure and properties of zirconium alloys—A review, Nucl. Eng. Technol. 47 (2015) 323–331, https://doi.org/10.1016/j.net.2014.12.015.
[40] L. Tournadre, F. Onimus, J.-L. Béchade, D. Gilbon, J.-M. Cloué, J.-P. Mardon, X. Feaugas, Toward a better understanding of the hydrogen impact on the radiation induced growth of zirconium alloys, J. Nucl. Mater. 441 (2013) 222–231, https://doi.org/10.1016/j.jnucmat.2013.05.045.